Split Hubbard bands at low densities

Daniel Hansen, Edward Perepelitsky, and B. Sriram Shastry

Physics Department, University of California, Santa Cruz, California 95064, USA

We present a numerical scheme for the Hubbard model that throws light on the rather esoteric nature of the upper and lower Hubbard bands, which have been invoked often in literature. We present a self-consistent solution of the ladder-diagram equations for the Hubbard model, and show that these provide, at least in the limit of low densities of particles, a vivid picture of the Hubbard split bands. We also address the currently topical problem of decay of the doublon states that are measured in optical trap studies, using both the ladder scheme and also an exact two-particle calculation of a relevant Green's function.

I. MOTIVATION AND INTRODUCTION

Hubbard's introduction of split bands in Ref. [1], i.e., the so-called upper Hubbard band (UHB) and the lower Hubbard band (LHB), is one of the most important qualitative ideas in the theory of correlated electrons. Their origin is the idea that since the energy levels of the atomic limit show two sets of states, one at $\omega \sim 0$ and another at $\omega \sim U$ as in Eq. (8) below, the formation of a crystal would broaden these levels into two sets of sub-bands. These sub-bands were originally discussed by Hubbard using a nonperturbative technique, which has the advantage of being exact in the limit of vanishing bandwidth $W \to 0$, i.e., the atomic limit. However, the technique failed to produce a Fermi liquid for weak couplings, as one expects physically. This failure led to severe early criticism of Hubbard's work.[2] The problem of reconciling Fermi liquids with the local picture developed by Hubbard, leading to the split bands, is of great importance in the physics of strong correlations. The one exception is the dynamical mean-field theory that gives a good account of the sub-band formation, especially in the proximity of half-filling.[3,4] However, away from half-filling, the picture is obscure and remains largely unresolved. It is this task that we address in this paper. We study the ladder diagrams that are argued to be exact at low densities, sharpen the argument for their validity in terms of the self-energy, and show that, at least in this limit, the concept of the split bands is completely consistent with the Fermi liquid picture. The numerical solution of the ladder diagrams is carried out in a self-consistent way and shows the emergence of the Hubbard split bands for large enough U/W. These merge for weak couplings and our results give a vivid picture of the crossover from weak to intermediate to strong coupling. While we can not access the physically important regime near half-filling, our results throw light on the nature of the Green's functions and the momentum occupation numbers that are unavailable by other means.

The self-energy is momentum and also frequency dependent in the ladder scheme and, for low densities, provides a full picture of the renormalization processes that occur at arbitrarily large interaction scale U. In particular, we see that the spectral function shows a low-lying feature and a high-energy $\sim O(U)$ feature, with spectral weights that are equal to $1 - \frac{n}{2}$ and $\frac{n}{2}$, respectively. It is seen that every

single added particle thus depletes the weight of the LHB and adds to the UHB, thereby accomplishing a "long-range spectral transfer," which has been described in literature as "Mottness."[5,6]

The momentum-space occupancy $m(k) = \langle c_{k\sigma}^\dagger c_{k\sigma} \rangle$ is computed and it is usefully broken up into three parts [Eq. (16)]: the occupied part $m_1(k)$ in Eq. (16), corresponding to occupied states that are automatically inside the LHB, the unoccupied LHB part $m_2(k)$ corresponding to unoccupied LHB states, and the unoccupied UHB part $m_3(k)$. In the limit of $U \to \infty$, only m_1 and m_2 survive, and this projection gives an exact view of the physics of the t-J model as well in the low-density limit. At low densities, we find that the ladder diagrams lead to a Luttinger-Ward compliant Fermi surface, and this Fermi surface survives the limit $U \to \infty$. Thus, even in this limit of extreme correlations $U \to \infty$, adiabatic continuity to the Fermi gas holds. Therefore, we have a useful and concrete alternative to the extreme coupling ideas proposed in work by one us,[7] where a different Fermi volume emerges at *all densities*, including the lowest ones.

One contemporary context for the Hubbard split bands is the problem of high-T_c superconductors; here, Anderson[8] has eloquently argued that, for large U, one can confine attention to carriers in the LHB, with the UHB pushed out of the range of relevant states. Given this projection to the LHB, the charge carriers inherit exotic properties such as spin charge separation, and also a new interaction, namely, the super exchange that comes with a scale of t^2/U. We see that at least at low densities where the ladder scheme is valid, the LHB does separate out cleanly for $U \geqslant W$, but the carriers are yet subject to Fermi liquid behavior.

Another recent context for motivating this work is the study of the Hubbard model far away from equilibrium with cold atom realization,[9,10] where the carriers in the UHB are optically excited, and their lifetime studied by measuring the overlap of the excited state with the initial state. We find that a calculation of a related correlation function is possible in the Fermi liquid at low densities, albeit in a close to equilibrium situation unlike the experiments. We are also able to exhibit the correlation function exactly for a pair of particles in the Hubbard band. Interestingly, the resulting lifetimes show some similarity in functional dependence to those found in experiment, although with a very different time scale.

II. LADDER-SCHEME EQUATIONS AT LOW DENSITY

The ladder scheme for the Green's function (Refs. [11–13], [14], and [15]) corresponds to convoluting a particle-particle ladder scattering amplitude $\Gamma(Q)$ with a single Green's function $G(k)$ to form the self-energy $\Sigma(k)$ as follows:

$$\Gamma(Q) = \frac{U}{1 + U\Pi(Q)},$$

$$\Pi(Q) = \frac{1}{\beta N_s} \sum_p G(p)G(Q - p), \tag{1}$$

$$\Sigma(k) = \frac{1}{\beta N_s} \sum_p G(p)\Gamma(k + p).$$

Here, N_s, N_e are the number of sites and electrons, $n = N_e/N_s$ is the electron number density, and we use the notation $k = (\vec{k}, i\omega_k)$ with imaginary odd frequencies $\omega_k = \pi \frac{1}{\beta}(2k + 1)$ of the finite-temperature field theory[16] for fermions, and reserve the capital letters for bosonic frequencies, e.g., $Q = (\vec{Q}, i\Omega_\nu)$ and $\Omega_\nu = 2\pi \frac{1}{\beta}\nu$. Here, the summation over p represents a sum over the vector component and also the imaginary frequency. A paramagnetic state is assumed and the spin label is suppressed for brevity. In addition to Eq. (1), we have the Dyson equation $G^{-1}(k) = G_0^{-1}(k) - \Sigma(k)$ with the usual noninteracting Green's function $G_0^{-1}(k) = i\omega_k - \varepsilon_k + \mu$. Thus, the ladder scheme is a self-consistent nonlinear scheme that needs to be solved numerically for the various objects $G(k)$, $\Sigma(k)$, and $\Pi(K)$. We can solve for the Dyson equation in the ladder scheme iteratively:

$$
G^{-1}(k) = G_0^{-1}(k) \\
- \frac{1}{\beta N_s} \sum_p G(p) \frac{U}{1 + \frac{U}{\beta N_s} \sum_q G(q)G(k + p - q)}. \tag{2}
$$

For example, in the first step, we can calculate the scattering amplitude (and self-energy) using G_0 and use Dyson's equation to obtain a new Green's function we call G_1:

$$
G_1^{-1}(k) = G_0^{-1}(k) - \frac{1}{\beta N_s} \\
\times \sum_p G_0(p) \frac{U}{1 + \frac{U}{\beta N_s} \sum_q G_0(q)G_0(k + p - q)}. \tag{3}
$$

We may continue and compute $G_2(k)$ using $G_1(k)$ to recompute the self-energy [i.e., the second term in Eq. (3)], and repeat this process iteratively to obtain $G(k) = \lim_{n\to\infty} G_n(k)$. The difference between $G_1(k)$ and the fully self-consistent $G(k)$ arises from the repeated renormalizations implicit in the full equations, and this brings about the self-consistent broadening of several sharp features that arise in $G_1(k)$. In Fig. 3, we discuss the difference in the spectral functions from these two theories as an illustration of this phenomenon.

Alternatively, we start by introducing spectral representations for the various quantities of physical interest[16,17]:

$$G(\vec{k}, i\omega_k) = \int d\nu \frac{\rho_G(\vec{k}, \nu)}{i\omega_k - \nu},$$

$$\Sigma(\vec{k}, i\omega_k) = U\frac{n}{2} + \int d\nu \frac{\rho_\Sigma(\vec{k}, \nu)}{i\omega_k - \nu}, \tag{4}$$

$$\Gamma(\vec{Q}, i\Omega_Q) = U + \int d\nu \frac{\rho_\Gamma(\vec{Q}, \nu)}{i\Omega_Q - \nu}.$$

The spectral functions $\rho_\Gamma(\vec{Q}, \nu)$, etc., have a compact support and are therefore convenient for numerical integration on a suitably discretized grid of frequencies. The numerical solution is performed after using a spectral representation for various physical quantities. We first turn the Dyson Eq. (2) into a nonlinear integral equation for the spectral function from Eq. (4) as follows:

$$
\rho_\Sigma(\vec{k}, \omega) = \frac{1}{N_s} \sum_{\vec{p}} \int d\nu \, \rho_G(p, \nu) \, \rho_\Gamma(\vec{p} \\
+ \vec{k}, \nu + \omega) \, [f(\omega) + n_B(\omega + \nu)],
$$

$$
\rho_\Pi(\vec{Q}, \Omega)) = \sum_{\vec{q}} \int d\nu \, \rho_G(q, \nu) \, \rho_G(Q - q, \Omega - \nu) \, [f(\nu) \\
+ f(\Omega - \nu) - 1],
$$

$$
\rho_\Gamma(\vec{Q}, \Omega) = \frac{-U^2 \rho_\Pi(\vec{Q}, \Omega)}{[1 + U\mathrm{Re}\Pi(\vec{Q}, \Omega)]^2 + [\pi U\rho_\Pi(\vec{Q}, \Omega)]^2}, \tag{5}
$$

with $f(\omega)$ and $n_B(\omega)$ as the Fermi and Bose distribution functions $[\exp \beta\omega \pm 1]^{-1}$, and $\mathrm{Re}\Pi(\vec{Q}, \Omega)$ defined as the Hilbert transform of $\rho_\Pi(\vec{Q}, \nu)$, i.e.,

$$\mathrm{Re}\Pi(\vec{Q}, \Omega) = \mathcal{P} \int d\nu \frac{\rho_\Pi(\vec{Q}, \nu)}{\Omega - \nu}.$$

A. Low-density limit and self-energy sum rule

The original argument for the ladder scheme[11,12] is that it is exact in the low-density limit. Specifically, the ground-state energy and some derived static quantities such as susceptibilities are argued to be exact. This argument is borrowed from the theory of nuclear matter, where Brueckner[18] originally argued that at any order n of perturbation theory for the ground-state energy (i.e., the Goldstone diagrams), the dominant diagrams are those with the smallest number of downward lines of holes. Topologically, there need to be at least two such hole lines in the free-energy diagrams. The particle-particle ladder diagrams have only two hole lines at any order. Thus, the ladder diagrams dominate all others at each order in perturbation theory. Importantly for nuclear matter, this logic shows that the large (divergent) two-body interaction is not a problem, it is cut off by these ladders, giving in the end an expansion in a dimensionless parameter obtained by combining the two-body scattering length with the average interparticle separation. A parallel argument for bosons was provided by Lee, Huang, and Yang.[19] The Kanamori- Galitskii papers implement this idea for the Feynman diagrams, where one has hole-hole scattering in addition to particle-particle ladders, for structural reasons that distinguish the Feynman from the Goldstone
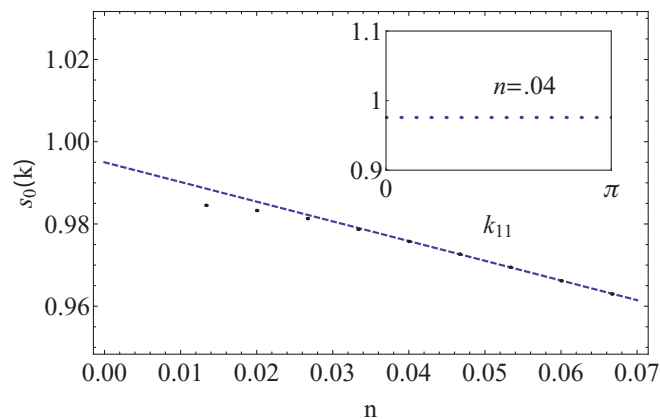
FIG. 1. (Color online) The zeroth moment of the self-energy versus the density normalized to the exact value $U^2\frac{n(2-n)}{4}$. These data are in two dimensions with $U = 10$, $W = 2$. The inset shows the k independence of the sum rule along the (11) direction for the case $n = 0.04$, with variations in the sixth significant figure.
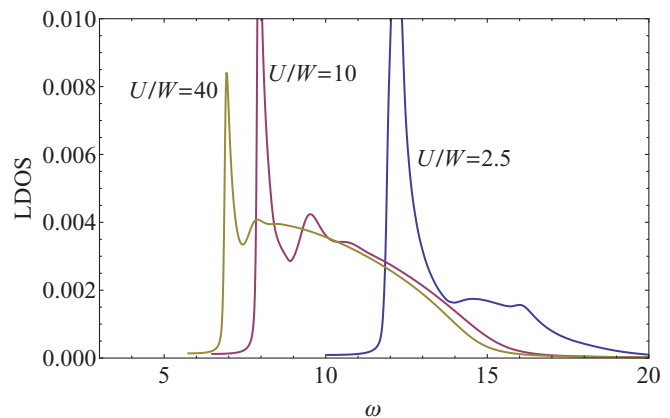

FIG. 2. (Color online) High-frequency (UHB) density of states in two dimensions, $n = 1/20$. As the hopping is decreased from $t = \frac{1}{2}, \frac{1}{8}, \frac{1}{32}$ at a fixed $U = 10$, the UHB consists of a sharp peak and a broad k-independent background that maintains a width of $O(U)$. The sharp k-dependent peak does narrow as the hopping decreases. In Fig. 3, the broad UHB of the full band can be seen with the G_1 from Eq. (3) superimposed. Here, the UHB feature is broadened by η and the LHB is suppressed for clarity.

diagrams. However, these extra terms do not detract from the particle-particle ladders that cohabit the Feynman series and provide a particular $O(n^2)$ correction term.

The reader would note that the above argument is rather indirect; in particular, it gives us no clue as to why we should accept the self-energy that emerges from this scheme as exact. In this context, it is useful to note that the self-energy satisfies an exact series of sum rules[6,20,21] of which the lowest is

$$s_0(k) \equiv \int d\nu\, \rho_\Sigma(\vec{k},\nu) = U^2\, \frac{n(2-n)}{4}, \qquad (6)$$

where the right-hand side is *independent of* $\vec{k}$. Note that this sum rule is valid for arbitrarily large U and at all densities. We can use this as a check of our calculation by testing for the $\vec{k}$ independence of the computed left-hand side, and also monitor its weight relative to the right-hand side. The self-consistent solution of the ladder diagrams contains the low-density limit and also provides some uncontrolled results at higher densities, and it is important to know the limit on density to which we can trust these results. Figure 1 gives details of this test for the ladder diagrams. For higher densities, the ladder-diagram theory is systematically wrong for the $O(n^2)$ term since we can show analytically that, at large U and low density, $s_0(k) = U^2\frac{n(1-n)}{2} + O(U)$ in contrast to Eq. (6). Our results for the self-energy thus provide a more stringent test for the ladder diagrams than, say, the ground-state energy, and show that there are systematic corrections already to first order in density to sum rules such as $s_0(k)$. We will see other examples of these deviations from exactness at low densities in several examples presented below, such as Fig. 7, and provide concrete limits to the extent to which one can trust the ladder scheme. On the positive side, however, the momentum independence of the sum rule, as seen in the inset of Fig. 1, is encouraging and suggests that the qualitative features of the ladder scheme are reliable at low densities.

B. Atomic limit

We discuss briefly the atomic limit, i.e., a limit where U remains finite but the bandwidth $W \to 0$. This limit is a

highly singular one since the ground state becomes enormously degenerate and is not expected to be reached in a smooth way from a finite hopping situation starting with a liquidlike state. However, this is a limit where one can solve for the Green's function exactly quite simply if one performs an unbiased average over all the degenerate ground states:

$$\Sigma_{\text{atomic}} = U\frac{n}{2} + U^2\, \frac{\frac{n}{2}\left(1 - \frac{n}{2}\right)}{i\omega + \mu - U\left(1 - \frac{n}{2}\right)}, \qquad (7)$$

$$G_{\text{atomic}} = \frac{1 - \frac{n}{2}}{i\omega + \mu} + \frac{\frac{n}{2}}{i\omega + \mu - U}. \qquad (8)$$

The breakup of the Green's function into two parts, with energies ~ 0 or $\sim U$ and weights $1 - n/2$ and $n/2$ is, of course, the fundamental factor that leads one to the picture of upper and lower Hubbard bands. Hubbard's contribution[1] was to provide a Green's function for finite hopping W using an equation-of-motion method that extended the atomic limit, although the details of his treatment came in for severe criticism[2] due to the failure of his scheme to ever yield a Fermi liquid with the Luttinger-Ward[22] ordained Fermi surface. It is interesting to study the $t \to 0$ limit in the present scheme of ladder diagrams in Fig. 2 where the local density of states $\frac{1}{N_s}\sum_k \rho_G(k,\omega)$ is shown for various values of U/W. We observe a sharp peak accompanied by a broad background term of width $O(U)$ that remains intact as $t \to 0$.

C. Emergence and structure of the split bands of Hubbard

In the ladder diagrams, it is straightforward to identify the origin of the upper Hubbard band: the scattering amplitude $\Gamma(Q)$ at frequencies $\Omega_Q \sim U$ has a pole in the first iteration, i.e., at the level of G_1 with

$$\Gamma_1(Q) \equiv \Gamma(Q;[G_0]) \sim \frac{U^2(1-n)}{i\Omega - U(1-n)}. \qquad (9)$$
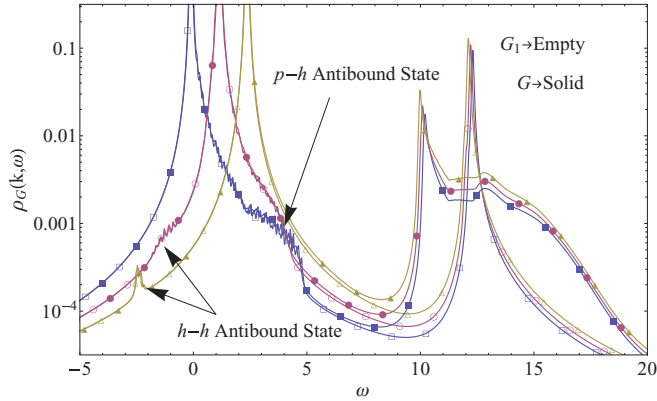
FIG. 3. (Color online) Two dimensions, $U = 10$, $W = 2.5$, and $n = 1/20$. The spectral function at three values of the wave vector $(0,0)$, $(\frac{\pi}{2},\frac{\pi}{2})$, (π,π) in blue (square), red (circle) and gold (triangle) colors. Aside from the quasiparticles, we observe three features emerging in each spectral function. Most obvious is the UHB feature that lies at a $\omega \approx O(U)$ and integrates to a weight of $n/2 + O(n^2)$. This feature is dramatically broadened in the self-consistent G also becoming less k dependent. On each edge of the quasiparticle band, we observe small dispersing features. Reference 15 has previously identified the negative frequency feature as a two-hole antibound state, while Ref. 24 has discussed a particle-hole antibound state just above the quasiparticle band. These features are essentially unchanged in going from G_1 from Eq. (3) to the exact G.

This pole was noted very early in works (Refs. 13 and 23) that identified this pole as the origin of strong correlations and Gutzwiller-type factors. In Fig. 3, we see that the spectral function obtained from the first iteration, i.e., G_1, shows a sharp feature at a higher energy of $O(U)$ that arises from this pole. This peak disperses and may be viewed as a "baby version" of the upper Hubbard band. Next, a self-consistent treatment of this theory with $\Gamma(Q;[G])$ evaluated with G (rather than G_0) broadens the upper band substantially, as seen in Fig. 3. It is interesting that the lower Hubbard band, i.e., the structure at energies below U, is stable with respect to the iterations, and is hardly different between the first iteration scheme and the final one.

We also see in Fig. 3 the existence of two features that have been commented upon in literature. The feature near the band bottom that disperses is the so-called hole-hole bound state noted by Randeria and Englebrecht (Ref. 15), whereas the hump near the leading edge is a particle-hole bound-state feature noted by Anderson (Ref. 24). These features coexist with the other, dominant ones, namely, the quasiparticle peak of the Fermi liquid and the broadened upper Hubbard band peak. If we replace the log-linear scale in Fig. 3 with a linear-linear scale as in Fig. 6, the UHB becomes almost negligible compared to the LHB feature.

D. Frequency-dependent self-energy

We next display the self-energy in the ladder scheme. The spectral density for the self-energy is given in Eq. (5), and it
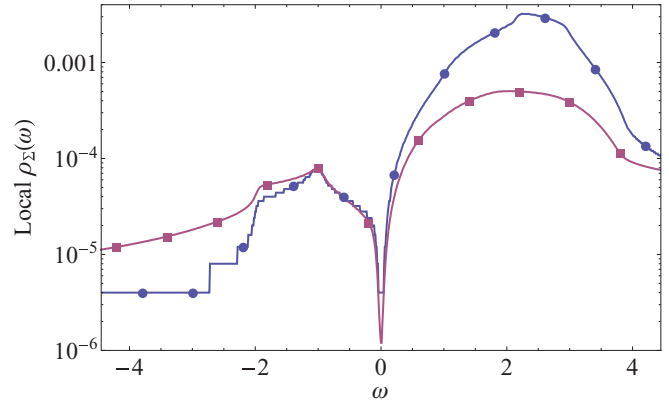

FIG. 4. (Color online) Two dimensions, $U = 0.25$, $U = 10$, $W = 2$, and $n = 0.049$. The local $\rho_\Sigma(\omega)$ divided by U versus ω. The two chosen values of U are in the weak-coupling (blue (circle) $U = 0.25$) and strong-coupling (red (square) $U = 10$) ranges, respectively. We see at the lowest temperatures that the the self-energy curves overlap when scaled by U displaying a characteristic quadratic dip at the chemical potential.

is possible to obtain an equation for its momentum sum, i.e., a local self-energy density

$$\frac{1}{N_s} \sum_k \rho_\Sigma(k,\omega) = \int d\nu \rho_{G,\text{loc}}(\nu)\rho_{\Gamma,\text{loc}}(\nu + \omega)$$

$$\times [f(\omega) + n_B(\omega + \nu)]. \quad (10)$$

For comparison, we note that the local self-energy in the atomic limit considered in Sec. II B is given by a single delta function centered at $U(1 - \frac{n}{2}) - \mu$ as

$$\rho_{\Sigma, \text{atomic}}(\omega) = U^2 \frac{n}{2}\left(1 - \frac{n}{2}\right)\delta\left[\omega - U\left(1 - \frac{n}{2}\right)\right]. \quad (11)$$

We also note the form of this object for a Fermi liquid at finite T:

$$\rho_{\Sigma, \text{local}}^{\text{Fermi liquid}}(\omega) = a\,\omega^2 + f_{\text{background}}(\omega), \quad (12)$$

a simple second-order self-consistent theory (corresponding to truncating the ladders at the first rung) gives the picture of this in a Fermi liquid (Fig. 4).

We see in Fig. 5 that the ladder scheme inherits both a quadratic minimum at $\omega = 0$ from the Fermi liquid and a large and broad feature near $\omega \sim U$ from the emergent Hubbard upper band. The inset emphasizes the Fermi liquid aspect, and the reader will observe that the absolute scale of this function is dominated by the UHB feature. In Fig. 6, the density of states (DOS) of the Green's function $\rho_G(\vec{k},\nu)$ is illustrated, along with the real and imaginary parts of the self-energy. The small feature in the DOS at the energy scale U is the UHB. We see that the real and imaginary parts of the self-energy reflect its presence in a profound fashion, which would be hard to guess from the size of the peak. In detail, it is interesting that the real part of the self-energy does display a linear behavior in ω with a known slope as one expects in the intermediate frequency range $0 \ll \omega \ll U$ from the theory of extremely correlated electronic systems in Refs. 7 and 25.

When $W = 0$, the UHB has a weight that is independent of momentum. However, for finite W, momenta near the top
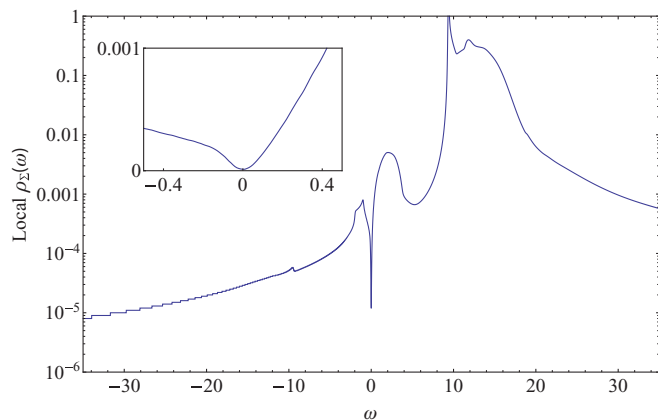
FIG. 5. (Color online) The local self-energy spectrum in two dimensions, $U = 10$, $W = 2$, and $n = 0.05$. The log-scale plot shows the full scale of the UHB. The inset highlights the quadratic minimum at low energies. The quadratic minimum drops below the scale of η, so it can be said to represent an infinite lifetime.

of the band will transfer weight more readily to the UHB. Figure 7 illustrates this progression. We show in Fig. 8 that the behavior of the local spectral function $\langle \rho_\Gamma(\vec{Q}, \nu) \rangle_Q$ closely follows that of the local self-energy $\rho_\Sigma(\nu)$.

If we look at large ω such that we can make the approximation $\omega + \nu \approx \omega$, the integral for $\rho_\Sigma(k, \omega)$ in Eq. (5) reduces to

$$\frac{1}{N_s} \sum_k \rho_\Sigma(k, \omega) \sim \frac{n}{2} \rho_{\Gamma, \text{loc}}(\omega), \tag{13}$$
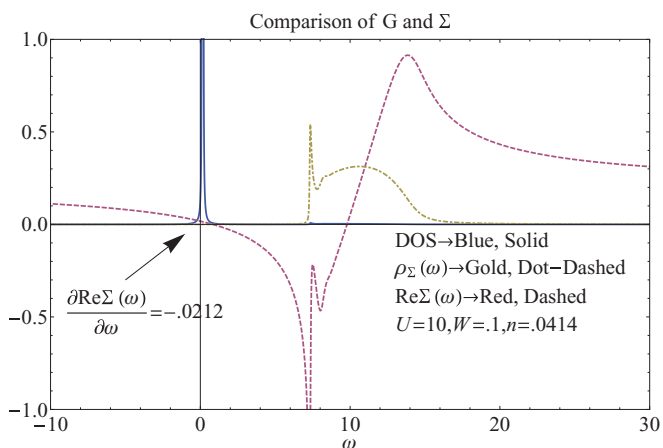
accounting for the similarity of these in Fig. 8.

FIG. 6. (Color online) The two-dimensional DOS, i.e., the momentum-averaged spectral function $\rho_G(\vec{k}, \nu)$ and the momentum-averaged $\rho_\Sigma(\vec{k}, \nu)$. The LHB feature is the sharp peak near $\omega \sim 0$. The UHB feature in the DOS is nearly invisible here but lies just below the feature in ρ_Σ scaled down by a factor of ω^2. The real part of the self-energy for $\omega \geqslant 0$ initially drops linearly with frequency over a range $W \ll \omega \sim \frac{U}{2}$, as required in the limit of extreme correlations (Refs. 7 and 25). It then flips at the threshold of the UHB, rising across the range of the UHB until, at the highest energy, it begins to decay down toward the Hartree term at infinite energy.
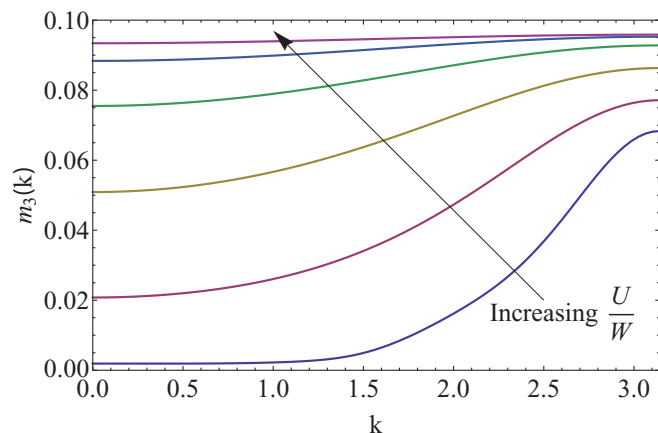

FIG. 7. (Color online) The integrated spectral weight over the UHB is called $m_3(k)$. It is plotted here for $\frac{W}{U} = 1.6$, 0.56, 0.196, 0.0686, 0.024, and 0.0085. In this case, $n = 0.15$. We observe that the weight of the UHB exceeds $n/2$ by $O(n^2)$ and becomes flat as U/W tends to infinity.

E. Momentum occupancy

We next turn to the momentum occupancy $m_k = \langle c^\dagger(k) c(k) \rangle$; this can be obtained from the Green's function or $\rho_G(k, \nu)$ by integration over the frequencies. In order to understand and illustrate the nature of the LHB and UHB breakup of this important object, we carry out the integration up to the center of the Hubbard-Mott gap. Thus, we define three objects $m_j(k)$ (with $j = 1, 2, 3$):

$$m_1(k) = \int_{-\infty}^{0} d\omega \, \rho_G(k, \omega), \tag{14}$$

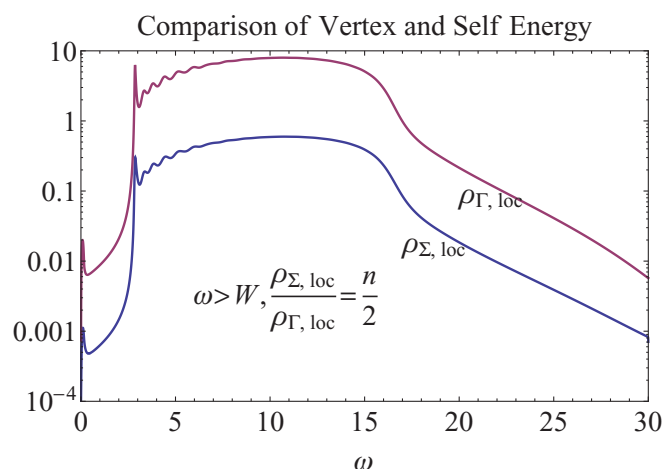$$m_2(k) = \int_{0}^{\omega_g} d\omega \, \rho_G(k, \omega), \tag{15}$$

FIG. 8. (Color online) From the convolution structure of $\rho_\Sigma(k, \omega)$, we see that the local objects of Σ and Γ are related by the ratio $n/2$ when $\omega > W$ for all values of W/U. In the strong-coupling limit, where the upper band is essentially independent of k, this relationship will be approximately true for each wave vector. On the negative frequency side, the thermal function acts differently such that the ratio for $\omega < -W$ is approximately $(1 + \frac{n}{2})$.
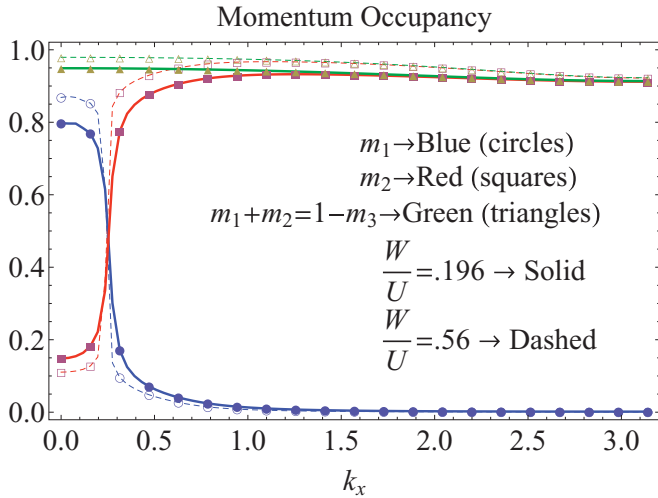
FIG. 9. (Color online) One-dimensional $U = 10$, $W = 0.56$ (dashed line), $W = 0.196$ (solid line), $n = 0.15$, and $\mathrm{T} = 0.005$. Here, m_1 is essentially the zero-temperature quasiparticle occupation, while m_2 accounts for the LHB particle addition spectrum. The sharp step in occupation occurs precisely at the Luttinger Fermi surface, which satisfies the Luttinger-Ward sum rule. The sum of m_1 and m_2 is less than one due to the weight transferred to the upper band. The total lower band weight approaches $1 - n/2$ as U/W goes to infinity.

$$m_3(k) = \int_{\omega_g}^{\infty} d\omega \, \rho_G(k, \omega). \quad (16)$$

Here, $m_1(k)$ represents the momentum-space occupancy of the occupied states that lie below the chemical potential. These are automatically in the LHB for energetic reasons and satisfy the sum rule $\sum_k m_1(k) = n/2 \times N_s$ with a sum over the entire Brillouin zone (BZ). Next, $m_2(k)$ represents the LHB contribution to the unoccupied states since the chemical potential lies within the LHB. If we send $U \to \infty$, then we are left with only the LHB, and in that limit, we expect the sum $m_1(k) + m_2(k) = 1 - \frac{n}{2}$ pointwise at each k. However, for finite but large U, this sum differs from $1 - \frac{n}{2}$ by terms of $O(t/U)$, and the UHB comes into play. Indeed, $m_3(k)$ refers to precisely the UHB contribution to the momentum occupation, and its momentum average over the BZ is $\frac{n}{2}$. These are displayed for typical parameters in Fig. 9. The sum of all three m functions should add to unity for each wave vector. However, due to the finite frequency resolution of our numerics, this sum rule is only approximately satisfied. We limit the error to $< 1\%$ by reducing our frequency step $d\omega$. The error is concentrated near k_f, where the spectral function is sharpest.

In Fig. 9, we display the k dependence of the three occupancy functions for a typical set of parameters. It is clear that the Luttinger-Ward Fermi surface controls the variations of the functions m_1 and m_2, which complement each other so that the sum is almost a constant.

III. DOUBLONS AND THEIR DYNAMICS

A. Doublon decay in the low-density limit

In recent experiments,[9,10] the lifetime of doublons created by optical excitation of the trapped atoms has been measured,

providing us with an added impetus for this study. The experiments actually study the decay of a highly nonequilibrium initial state $|\psi_{\mathrm{initial}}\rangle$ with *a finite fraction of excited doublons*, i.e., $\langle \psi_{\mathrm{initial}} | \hat{D} | \psi_{\mathrm{initial}} \rangle \propto N_s$, where the doublon number $\hat{D} = \sum_i n_{i\uparrow} n_{i\downarrow}$. The object studied is the time evolution of such a state followed by a measurement of D and then a projection on to the evolved state, i.e.,

$$\xi(t_r) = \langle \psi_{\mathrm{initial}} | \exp\{i t_r H\} \, \hat{D} \, \exp\{-i t_r H\} | \psi_{\mathrm{initial}} \rangle. \quad (17)$$

Here and below, we use the symbol t_r to denote real (Schrödinger) time, thus distinguishing it from the band hopping parameter t. Such a correlation function is not usually amenable to study near-equilibrium-type situations studied in many-body physics. The initial state is itself quite far from being an equilibrium (ground) state. However, in the limit of very low densities, one can approximately view the initial state as the vacuum or few-particle state with a few doublon excitations; within this picture, we may ask how a single doublon decays. This is roughly the question of the lifetime of a state in the upper Hubbard band, and thus related to our general theme in this paper.

We are able to calculate the lifetime of a doublon within the ladder scheme and, hence, presumably an exact answer at low densities as argued here. We next provide a discussion of the function γ in a low-density Fermi liquid. We start with the correlation function defined for Matsubara time $\tau \geqslant 0$ in terms of the two-particle Green's function[16]

$$\gamma(r, \tau) \equiv G^{\mathrm{II}}_{\uparrow, \downarrow, \downarrow, \uparrow}(r\tau, r\tau; 0, 0)$$
$$= \langle c_{r,\uparrow}(\tau) c_{r,\downarrow}(\tau) c^{\dagger}_{0,\downarrow}(0) c^{\dagger}_{0,\uparrow}(0) \rangle, \quad (18)$$

and an analogous expression for real times $\gamma(r, t_r)$. This object can be expressed in terms of the scattering amplitude[26] as

$$\gamma(r, t_r) = \sum_Q \int d\Omega \, \rho_\Gamma(Q, \nu)[1 + n_B(\nu)] e^{-iQr - i\nu t_r}. \quad (19)$$

In Fig. 10, we display $\gamma(0, t_r)$ within the ladder scheme. As the density is increased, the UHB becomes broader and less k dependent; however, sharp k-dependent features persist with weight that decreases as t/U goes to zero. The k-dependent pieces remain sharp and determine the rate of the long-time exponential decay. On the other hand, the k-independent pieces, being broad, determine the short-time decay. Due to our finite frequency resolution, these numerics do not see the long-time exponential decay becoming infinitely long once $t < \eta$.

We have also computed the off-site correlation function $\gamma(1, t_r > 0)$; Fig. 11 shows that even the site directly adjacent to the created doublon has a very small amplitude.

B. Exact solution of the doublon decay problem for two particles

In addition to the discussion of the low-density case, we are able to solve exactly the admittedly simple problem of the dynamics of a single doublon in the Hubbard model, and from this study provide some feeling for the validity of the ladder scheme. The single doublon problem is solvable since, for two particles of opposite spin, we have a total momentum quantum
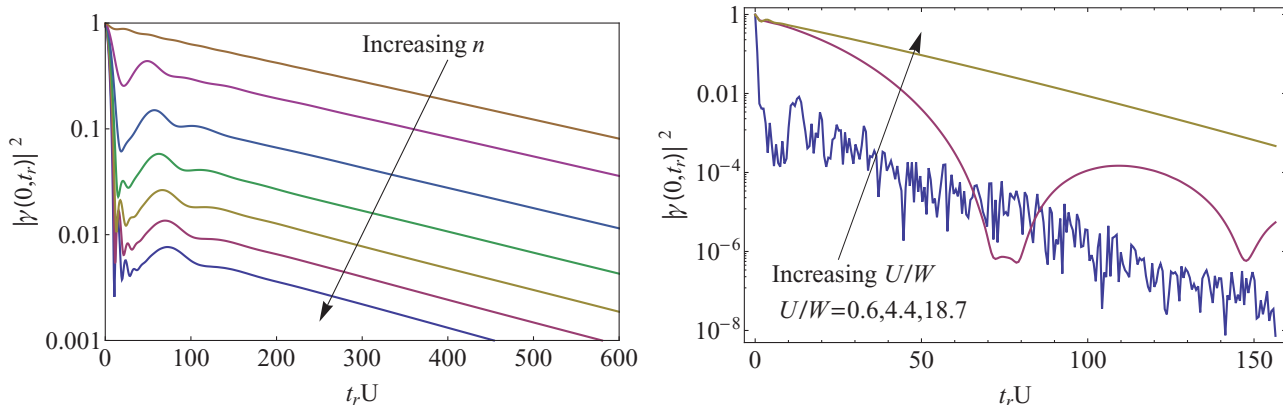
FIG. 10. (Color online) The doublon dynamics breaks into two regimes: a sharp decay at early times followed by a long exponential tail. The magnitude of the initial decay depends strongly on the density. In the limit $n \to 0$, the initial decay disappears, indicating that the UHB is comprised of sharp features only in the limit of vanishing density. In the right panel, the U dependence of the long-time decay is shown, it slows down, and is finally limited by the level broadening η assumed in our numerics. Here, γ consists of a UHB piece and a LHB piece that interfere, causing oscillations. For large U/W, the LHB piece becomes small and, hence, there is no interference.

number and, in each sector of this, we have a single-particle-type Schrödinger equation to solve. Let us first outline this problem and its solution with regard to the correlation function

$$\gamma(r,t_r) = \langle 0 | c_{r,\uparrow}(t_r) c_{r,\downarrow}(t_r) c_{0,\downarrow}^{\dagger}(0) c_{0,\uparrow}^{\dagger}(0) | 0 \rangle. \quad (20)$$

Here, the average is with respect to the vacuum state with no particles, although below we will use the average over the thermal distribution function for a low-density Fermi liquid. In the case of two particles, it is in fact possible to show that $\gamma(r,t_r)$ is related to the correlator $\xi(t_r)$ in Eq. (17) exactly through

$$\xi(t_r) = \sum_r |\gamma(r,t_r)|^2. \quad (21)$$

This follows upon using the fact that, with only two particles in the system, the destruction operator $c_{r,\uparrow}(t_r) c_{r,\downarrow}(t_r)$ can only connect to the vacuum state. We expect this relation to be only approximately true for a dense Fermi system but useful since it can be computed with relative ease by one of several techniques. It is also dominated by the term $r = 0$, as shown explicitly below in Fig. 11, and hence it is useful to regard $|\gamma(0,t_r)|^2$ as an estimator of $\xi(t_r)$.

Reference 10 estimates $\gamma(0,t_r)$ by an argument that is appropriate in an incoherent Fermi system, and argue that this function decays on a time scale that is given as

$$\frac{h}{\tau} = At \exp\left\{-B\frac{U}{W}\right\}. \quad (22)$$

The vanishing of the rate as $W \to 0$ is expected in view of the conservation of the doublon number in the absence of electron hopping, the coefficients are estimated from experiments on the three-dimensional cubic lattice ($W = 12t$) as $A \sim 0.9 \pm 0.5$ and $B \sim 1.6 \pm 0.16$.

For the two-particle problem, we have exact analytical and numerical solutions. In the interesting case of $U > W$ in d-dimensional hypercubes with nearest-neighbor hopping, we

can write

$$\gamma(0,t_r) = \gamma_L(0,t_r) + \gamma_U(0,t_r),$$
$$\gamma_U(0,t_r) \sim e^{-i(U+4d\frac{t^2}{U})t_r} J_0^d\left(\frac{4t^2}{U}t_r\right), \quad (23)$$

where the LHB contribution $\gamma_L \sim O\big((W/U)^2\big)$ and negligible. The second term arises from the UHB, and for intermediate $W \ll U$, is related to the Bessel function J_0 whereby it decays as a power law rather than as an exponential. This is understandable since the two-body problem is an integrable system, and we expect that, in the low-density limit, this power law would be replaced by an exponential-type decay. The function $|\gamma|^2$ can be found easily (see the Appendix) by numerical means, and Figs. 12 and 13 give us a picture of the decay.

In Fig. 14, we show that the half width at half maximum (HWHM) of the computed $\gamma(0,t_r)$ leads to a rate $\frac{\hbar}{\tau_{\text{HWHM}}}$, which
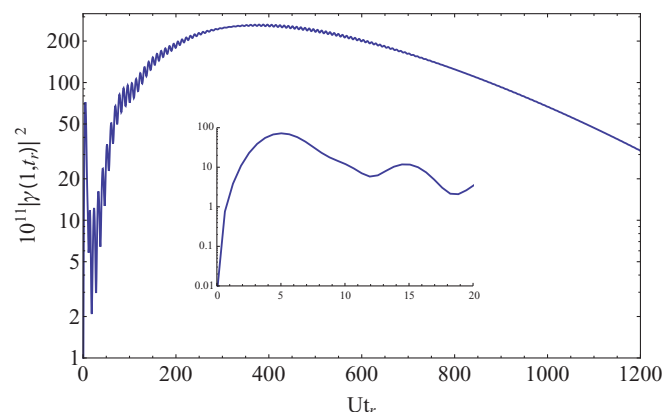

FIG. 11. (Color online) The inset shows that $\gamma(1,t_r)$ goes to zero at early times since there is no mechanism to hop at small times. On a longer time scale, we see the development of an exponential decay. The small magnitude of the correlation is due to fact that the UHB is largely k independent.
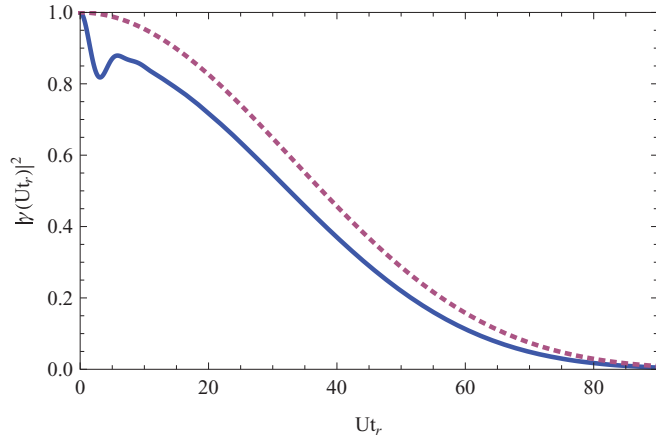
FIG. 12. (Color online) Doublon decay on a cubic lattice with $U = 15$ and $W = 12$. The shape of $|\gamma_U(Ut_r)|^2$ (red dashed curve) initially deviates slightly from the exact numerical result (blue curve) due to the neglect of the γ_L term, which decays much more quickly than the UHB contribution.

has a behavior that is similar to that in the experiments fit by Eq. (22).

IV. CONCLUSIONS

In conclusion, we have shown that the self-consistently computed ladder diagrams provide a detailed picture of the split bands for the Hubbard model. The UHB has a distinct shape that is captured here and related to the shape of the two-particle scattering amplitude. We have delineated how the lower Hubbard band occupation is influenced by the passage to large U. Here, the background momentum occupance found in variational studies of the Gutzwiller approximation[27] arises here dynamically. Finally, we have shown that the decay of the doublon in such a system can be calculated by the ladder diagrams as well as by exact methods for very low densities, and the shapes of these curves are fairly close to those found in recent experiments on atomic traps performed under very different physical conditions.
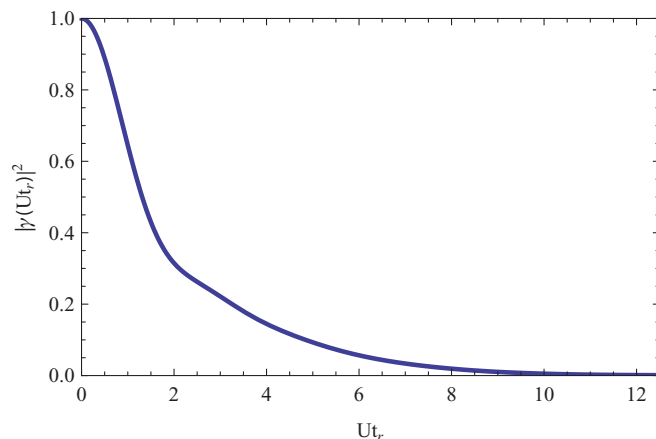

FIG. 13. (Color online) Doublon decay on a cubic lattice with $U = 5$ and $W = 12$. In the case $U < W$, it is much more difficult to find an exact analytical form, so only the numerical result is displayed.
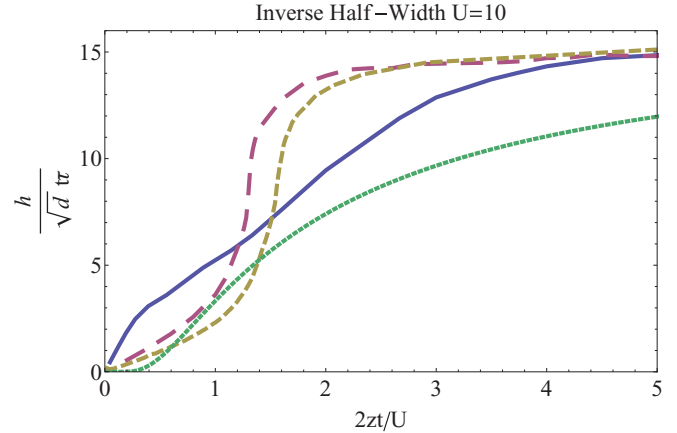

FIG. 14. (Color online) Two theoretical calculations, from ladder diagrams of Eq. (19) in two dimensions (Solid) and the exact two-particle solution from Eq. (21) and Eq. (A10) in two and three dimensions (long dash and short dash). These are compared to the experiment Eq. (22) in three dimensions (dot dash), scaled to coincide at weak coupling by a factor 26.4. The theory and experiment are in very different limits of physical parameters, but have a similar shape, except at large U/t.

APPENDIX: EXACT CORRELATION FUNCTIONS FOR THE TWO-PARTICLE HUBBARD MODEL

We consider the Hubbard model with two particles, one spin up and the other spin down. Our goal is to calculate the following correlation function:

$$\gamma(t_r) = \langle 0 \, | c_{i\downarrow} c_{i\uparrow} e^{-iHt_r} c_{i\uparrow}^\dagger c_{i\downarrow}^\dagger \, | 0 \rangle = \gamma_U(t_r) + \gamma_L(t_r).$$
(A1)

The two parts arise from intermediate states that are in the two split bands. Thus,

$$\gamma_U(t_r) = \sum_{\nu \in \text{UHB}} | \langle \nu \, | c_{i\uparrow}^\dagger c_{i\downarrow}^\dagger \, | 0 \rangle \, |^2 e^{-iE_\nu t_r},$$
$$\gamma_L(t_r) = \sum_{\nu \in \text{LHB}} | \langle \nu \, | c_{i\uparrow}^\dagger c_{i\downarrow}^\dagger \, | 0 \rangle \, |^2 e^{-iE_\nu t_r}.$$
(A2)

We now calculate the eigenvalues and eigenstates for the two-particle Hubbard model. As our basis, we take momentum eigenstates

$$| Q,k \rangle \equiv c_{Q-k\uparrow}^\dagger c_{k\downarrow}^\dagger \, | 0 \rangle,$$
(A3)

where Q is the total momentum of the state, and both Q and k can be any vector in the first Brillouin zone. The Hamiltonian acts on the basis in the following way:

$$H \, | Q,k \rangle = E_k \, | Q,k \rangle + \frac{U}{N_s} \sum_p | Q,p \rangle,$$
(A4)

where $E_k = (\epsilon_{Q-k} + \epsilon_k)$. The Hamiltonian conserves total momentum. Thus, we can diagonalize each total momentum sector independently. Each sector will have N_s eigenstates,

where N_s is the size of the lattice. We now fix Q and work in a particular total momentum sector. The basis states now depend on a single index k. The E_k's will in general be degenerate, and we take an E with degeneracy n, i.e., $\deg(E) = n$, corresponding to states $|Q,k_1\rangle, \ldots, |Q,k_n\rangle$. From these, we can make an $n-1$ dimensional degenerate eigenspace of the Hamiltonian with energy E, which we shall call $|\psi\rangle_{\text{deg}}$:

$$|\psi\rangle_{\text{deg}} = \sum_{i=1}^{n} \alpha_i |Q,k_i\rangle, \qquad \sum_i \alpha_i = 0. \qquad (A5)$$

One can see that these are eigenstates with energy E since the potential energy term goes to zero due to the condition $\sum_i \alpha_i = 0$ and the kinetic energy term gives E times the state. Suppose that there are p unique values of E in this total momentum sector:

$$\deg(E_1) + \cdots + \deg(E_p) = N_s. \qquad (A6)$$

By forming states in the way described above, we can obtain $N_s - p$ eigenstates $|\psi\rangle_{\text{deg}}$ that are independent of U. We obtain the remaining nontrivial (i.e., U dependent) p eigenstates by plugging the following state into the Hamiltonian:

$$|\psi_Q\rangle = \sum_k \Phi_Q(k) |Q,k\rangle \quad \text{and} \quad H|\psi_Q\rangle = \Lambda_Q |\psi_Q\rangle. \qquad (A7)$$

Here, we consider states with a fixed total momentum Q since this object is conserved. This yields the following results:

$$\Phi_Q(k) = \frac{1}{c_Q \sqrt{N_s}} \frac{1}{\Lambda_Q - E_k}, \quad c_Q$$
$$= \left(\frac{1}{N_s} \sum_k \frac{1}{(\Lambda_Q - E_k)^2}\right)^{\frac{1}{2}}, \quad \frac{U}{N_s} \sum_k \frac{1}{\Lambda_Q - E_k} = 1. \qquad (A8)$$

We can see explicitly from Eq. (A8) that $\langle \psi_Q | \psi\rangle_{\text{deg}} = 0$ since basis states with equal E have equal coefficients, and therefore the condition $\sum_i \alpha_i = 0$ makes this state orthogonal to the degenerate manifold of states in Eq. (A5). There are $p-1$ solutions of Eq. (A8) that lie in-between the p distinct E's. The corresponding states are in the lower Hubbard band. The $|\psi\rangle_{\text{deg}}$ found earlier also lie in the lower Hubbard band since these states are independent of U. There is one solution of Eq. (A8) for which $\Lambda_Q > E_{\max}$ and is of order U if $U > W$. The corresponding state lies in the upper Hubbard band. Thus, for each fixed Q sector, there is one state in the upper Hubbard band. We now consider the doublon state

$$|\psi\rangle_d = c_{i\uparrow}^{\dagger} c_{i\downarrow}^{\dagger} |0\rangle = \frac{1}{N_s} \sum_{Q,k} e^{-iQ \cdot R_i} |Q,k\rangle. \qquad (A9)$$

We can rewrite

$$\gamma(t_r) = \sum_Q |\langle \psi_Q | \psi\rangle_d|^2 e^{-i\Lambda_Q t_r}, \qquad (A10)$$

where the Q in the above sum stands for the p states described by Eq. (A8) in the total momentum sector Q. Since $\langle \psi_d | \psi\rangle_{\text{deg}} = 0$, we did not have to take the degenerate

states into account when calculating the correlation function. Furthermore, we see that

$$|\langle \psi_Q | \psi\rangle_d|^2 = \frac{1}{N_s c_Q^2 U^2}, \qquad (A11)$$

where c_Q is from Eq. (A8) and

$$\gamma_U(t_r) = \sum_{Q \epsilon \text{UHB}} \frac{1}{N_s c_Q^2 U^2} e^{-i\Lambda_Q t_r}. \qquad (A12)$$

In the above sum, each Q now represents only one state, since there is only one UHB state in each total momentum sector. We first evaluate this in one dimension, and then generalize to multiple dimensions. The sum can be turned into an integral

$$\gamma_U(t_r) = \frac{1}{\pi} \int_0^{\pi} \frac{1}{c_Q^2 U^2} e^{-i\Lambda_Q t_r} dQ. \qquad (A13)$$

By converting Eq. (A8) into integrals, we find that

$$\Lambda_Q = \left(U^2 + 16t^2 \cos^2 \frac{Q}{2}\right)^{\frac{1}{2}}, \qquad (A14)$$

$$c_Q^2 = \frac{1}{U^3}\left(U^2 + 16t^2 \cos^2 \frac{Q}{2}\right)^{\frac{1}{2}}. \qquad (A15)$$

For $U > W$, we keep corrections of $O(\frac{t^2}{U^2})$ in Λ_Q and drop all corrections in c_Q^2, yielding

$$\gamma_U(t_r) \sim \frac{1}{\pi} \int_0^{\pi} e^{-iU(1+8\frac{t^2}{U^2}\cos^2 \frac{Q}{2})t_r} dQ, \qquad (A16)$$

$$\gamma_U(t_r) \sim e^{-i(U+4\frac{t^2}{U})t_r} J_0\left(\frac{4t^2}{U} t_r\right). \qquad (A17)$$

In two dimensions, Eq. (A8) becomes an elliptic integral so there is no closed-form answer for the upper band eigenvalues in terms of elementary functions. However, for $U > W$, keeping corrections to the same order as we did in deriving Eq. (A16), we can easily generalize to higher dimensions

$$\Lambda_Q = U\left(1 + 8\frac{t^2}{U^2} \Sigma_{i=1}^d \cos^2 \frac{Q_i}{2}\right), \qquad (A18)$$

$$c_Q^2 = \frac{1}{U^2}, \qquad (A19)$$

$$\gamma_U(t_r) \sim e^{-i(U+4d\frac{t^2}{U})t_r} J_0^d\left(\frac{4t^2}{U} t_r\right). \qquad (A20)$$

The other contribution to $\gamma(t_r)$ is $\gamma_L(t_r)$. However, from degenerate perturbation theory, we know that provided $U > W$, $|\langle \nu | \psi\rangle_d|^2$ is $O(\frac{t^2}{U^2})$ smaller for $\nu \epsilon$ LHB than it is for the upper Hubbard band. Hence, $\gamma_L(t_r)$ is a small correction to $\gamma_U(t_r)$:

$$\gamma(t_r) \approx \gamma_U(t_r), \qquad (A21)$$

$$|\gamma(t_r)|^2 \approx J_0^{2d}\left(\frac{4t^2}{U} t_r\right). \qquad (A22)$$

In conclusion, the doublon decay in the two-particle Hubbard model in the regime $U > W$ is dominated by γ_U with the much faster decaying γ_L giving a small correction. To a good approximation, the shape of the decay of $|\gamma(t_r)|^2$ is $J_0^{2d}(\frac{4t^2}{U} t_r)$.

[1] J. Hubbard, Proc. R. Soc. London, Ser. A **276**, 238 (1963).

[2] C. Herring, in *Magnetism*, edited by G. T. Rado and H. Suhl (Academic, New York, 1966), Vol. 4.

[3] W. Metzner and D. Vollhardt, Phys. Rev. Lett. **62**, 324 (1989).

[4] Antoine Georges, Gabriel Kotliar, Werner Krauth, and Marcelo J. Rozenberg, Rev. Mod. Phys. **68**, 13 (1996).

[5] P. Phillips, T.-P. Choy, and R. G. Leigh, Rep. Prog. Phys. **72**, 036501 (2009); T. D. Stanescu and P. Phillips, Phys. Rev. B **69**, 245104 (2004).

[6] H. Eskes, M. B. J. Meinders, and G. A. Sawatzky, Phys. Rev. Lett. **67**, 1035 (1991).

[7] B. S. Shastry, Phys. Rev. B **81**, 045121 (2010).

[8] P. W. Anderson, Science **235**, 1196 (1987); *The Theory of Superconductivity* (Princeton University Press, Princeton, NJ, 1997).

[9] N. Strohmaier, D. Greif, R. Jordens, L. Tarruell, H. Moritz, T. Esslinger, R. Sensarma, D. Pekker, E. Altman, and E. Demler, Phys. Rev. Lett. **104**, 080401 (2010).

[10] R. Sensarma, D. Pekker, E. Altman, E. Demler, N. Strohmaier, D. Greif, R. Jordens, L. Tarruell, H. Moritz, and T. Esslinger, Phys. Rev. B **82**, 224302 (2010).

[11] V. M. Galtiskii, Zh. Eksp. Teor. Fiz. **34**, 151 (1958).

[12] J. Kanamori, Prog. Theor. Phys. **30**, 275 (1963).

[13] G. Horowitz and D. Jacobi, Phys. Rev. Lett. **29**, 1600 (1972).

[14] H. Fukuyama and Y. Hasegawa, Prog. Theor. Phys. Suppl. **101**, 441 (1990).

[15] J. R. Engelbrecht and M. Randeria, Phys. Rev. Lett. **65**, 1032 (1990).

[16] A. A. Abrikosov, L. Gorkov, and I. Dzyaloshinski, *Methods of Quantum Field Theory in Statistical Physics* (Prentice-Hall, Englewood Cliffs, NJ, 1963).

[17] G. D. Mahan, *Many Particle Physics*, 2nd ed. (Plenum, New York, 1991).

[18] K. A. Brueckner, Phys. Rev. **100**, 36 (1955).

[19] T. D. Lee, K. Huang, and C. N. Yang, Phys. Rev. **106**, 1135 (1957).

[20] A. B. Harris and R. V. Lange, Phys. Rev. **157**, 295 (1967).

[21] J. J. Deisz, D. W. Hess, and J. W. Serene, Phys. Rev. B **66**, 014539 (2002).

[22] J. M. Luttinger and J. C. Ward, Phys. Rev. **118**, 1417 (1960); J. M. Luttinger, *ibid*. **119**, 1153 (1960); **121**, 942 (1961).

[23] B. S. Shastry and T. M. Rice (unpublished).

[24] P. W. Anderson, Phys. Rev. Lett. **64**, 1839 (1990).

[25] In Ref. [7], Eq. (D4), it is argued that the real part of the self-energy in the range of frequencies $W \ll \omega \ll U$ must have the behavior $\mathrm{Re}\,\Sigma(\vec{k},\omega) = -\frac{n}{2-n}\omega + \mathrm{const}$. Hence, at a density $n = 0.0414$, we expect $\mathrm{Re}\,\Sigma(\vec{k},\omega) = -0.0212\omega + \mathrm{const}$., as found numerically.

[26] This is easy to see from the definition of the scattering amplitude and its result in the ladder scheme:

$$G^{\mathrm{II}}(Q,p_1,p_2) = G(Q/2+p_1)G(Q/2-p_1) - G(Q/2+p_1)$$
$$\times G(Q/2-p_1)\Gamma(Q)G(Q/2+p_2)G(Q/2-p_2),$$
$$\gamma(Q) = \sum_{p_1,p_2} G^{\mathrm{II}}(Q,p_1,p_2) = \frac{\Pi(Q)}{1+U\Pi(Q)},$$

where we used Eq. (1). The spectral density of γ is now easy to find,

$$\rho_\gamma = \frac{-\rho_\Pi}{(1+U\mathrm{Re}\Pi)^2 + (\pi U\rho_\Pi)^2},$$

leading to the quoted result.

[27] T. M. Rice and K. Ueda, Phys. Rev. B **34**, 6420 (1986).